2007

Mechanical and electronic properties of CdTe tetrapods studied by atomic force microscopy

Liang Fang

Jeong Young Park

Yi Cui

Joshua Schrier
Haverford College, jschrier@haverford.edu

AIP | The Journal of Chemical Physics

Mechanical and electrical properties of CdTe tetrapods studied by atomic force microscopy

Liang Fang, Jeong Young Park, Yi Cui, Paul Alivisatos, Joshua Shcrier et al.

Citation: J. Chem. Phys. **127**, 184704 (2007); doi: 10.1063/1.2786993
View online: http://dx.doi.org/10.1063/1.2786993
View Table of Contents: http://jcp.aip.org/resource/1/JCPSA6/v127/i18
Published by the American Institute of Physics.

Mechanical and electrical properties of CdTe tetrapods studied by atomic force microscopy

Liang Fang and Jeong Young Park
Molecular Foundry, Materials Science Division, Lawrence Berkeley National Laboratory, Berkeley, California 94720, USA

Yi Cui and Paul Alivisatos
Chemistry Department, University of California at Berkeley, Berkeley, California 94720, USA

Joshua Shcrier, Byounghak Lee, and Lin-Wang Wang
Computational Research Division, Lawrence Berkeley National Laboratory, Berkeley, California 94720, USA

Miquel Salmeron[a)]
Molecular Foundry, Materials Science Division, Lawrence Berkeley National Laboratory, Berkeley, California 94720, USA

(Received 26 January 2007; accepted 28 August 2007; published online 12 November 2007)

The mechanical and electrical properties of CdTe tetrapod-shaped nanocrystals have been studied with atomic force microscopy. Tapping mode images of tetrapods deposited on silicon wafers revealed that they contact the surface with three of its arms. The length of these arms was found to be 130 ± 10 nm. A large fraction of the tetrapods had a shortened vertical arm as a result of fracture during sample preparation. Fracture also occurs when the applied load is a few nanonewtons. Compression experiments with the atomic force microscope tip indicate that tetrapods with the shortened vertical arm deform elastically when the applied force was less than 50 nN. Above 90 nN additional fracture events occurred that further shortened the vertical arm. Loads above 130 nN produced irreversible damage to the other arms as well. Current-voltage characteristics of tetrapods deposited on gold revealed a semiconducting behavior with a current gap of ~ 2 eV at low loads (<50 nN) and a narrowing to about 1 eV at loads between 60 and 110 nN. Atomistic force field calculations of the deformation suggest that the ends of the tetrapod arms are stuck during compression so that the deformations are due to bending modes. Empirical pseudopotential calculation of the electron states indicates that the reduction of the current gap is due to electrostatic effects, rather than strain deformation effects inside the tetrapod. © *2007 American Institute of Physics*. [DOI: 10.1063/1.2786993]

I. INTRODUCTION

CdSe and CdTe nanocrystals possess interesting photoelectronic properties[1] that make them interesting materials for solar cell applications.[2] Branched tetrapods with a CdSe core and terminal CdTe branches are also important due to unusual charge-separation properties.[3–5] In addition to electronic properties, the peculiar shape of the nanocrystals might confer to these material interesting mechanical properties, such as large compliance and toughness, with potential applications as shock absorbers.

In this paper we present a study of the mechanical properties of individual CdTe tetrapods, including adhesion, compliance, and resistance to fracture. We will also present some results on the relationship between mechanical and electronic properties.

[a)]Author to whom correspondence should be addressed. Electronic mail: mbsalmeron@lbl.gov

II. METHODS

A. Experimental

CdTe tetrapods were synthesized using colloid chemistry.[2] The crystals were suspended in toluene with a concentration of 1 μM. The solution was used without further purification. For measurements of mechanical properties, the samples were spin casted from the toluene suspension onto a silicon wafer at a speed of 8000 rpm, followed by rinsing with pure methanol. For electrical measurements the tetrapods were deposited on a (111) oriented gold film on a glass substrate following a similar spin casting procedure. The Au substrate was prepared by annealing in a butane flame in air, after cleaning in acetone, chloroform, methanol, and piranha solution (2:3; H_2O_2:H_2SO_4). The resulting surface consisted of large grains exposing flat terraces of (111) orientation with sizes up to 400 nm, separated by monatomic steps.

To study the mechanical properties of the tetrapods the force-volume (FV) technique was used.[6–8] In this technique force-distance curves are acquired at each pixel of a selected

area imaged by the atomic force microscopy (AFM). From these curves adhesion and elasticity maps can be produced. The measurements were carried out with an Asylum Research MFP-3D AFM. The piezoscanner was calibrated in x, y, and z directions using NIST certified calibration gratings (MikroMasch). The spring constants of rectangular silicon cantilevers (Olympus) were determined from the thermal noise spectrum and found to range from 1.2 to 1.7 N/m. All experiments were performed under ambient conditions (21 ± 1 °C, 30% relative humidity). A loading speed of 200 nm/s was used in all force-distance measurements.

The electrical measurements were carried out in a RHK AFM operating in ultrahigh vacuum using cantilevers with a conductive TiN coating.[9] The spring constant of these cantilevers was measured to be 2.5 N/m using the method of Sader *et al.*[10]

B. Theoretical

To simulate the mechanical properties of the tetrapods, we used the valence force field (VFF) method containing nearest-neighbor bond stretching, bond-angle bending, and bond-length/bond-angle terms fitted to the experimental bulk elastic constants.[11] This type of classical model cannot handle bond breaking, therefore our calculations only concern the elastic regime in the experiment. The elastic constants (C_{11}, C_{12}, C_{44}) of our VFF model: $(5.48, 3.58, 1.89) \times 10^{10}$ N m^{-2} agree well with the experimental values $(5.35, 3.71, 2.02) \times 10^{10}$ N m^{-2} of bulk CdTe.[12] To model the compression of the tetrapod, the top and bottom boundaries of the system were treated as impenetrable planes perpendicular to the vertical arm of the tetrapod, which were then pushed together, minimizing the VFF total energy with respect to all atomic coordinates. We examined two possible cases: (i) the horizontal arms are allowed to slide freely on the bottom plane, modeling a scenario in which there is no sticking interaction with the surface; and (ii) the ends of the horizontal arms are fixed in place, modeling a scenario in which strong interaction with the surface prevents the ends of the arms from sliding. The numerical derivative of the energy (with respect to vertical displacement) gives the force.

We consider a CdTe tetrapod with arm diameter of 2.8 nm, horizontal arm lengths of 38 nm, and vertical arm length of 10.5 nm (containing 24 692 cation and anion atoms), i.e., the dimensions were reduced by a factor of 3 from the experimental one while keeping the same shape and aspect ratios. This is a compromise between making the system size large enough to be physically relevant and the computational cost, especially for the subsequent quantum mechanical calculations. Since the displacement distances will be smaller, we will instead compare the spring constants (force/displacement); and because the dimensional scaling is expected to follow Young's equation scaling, we will include a multiplicative factor of 3 when comparing to the experimental results.

To calculate the electronic structure of the tetrapod we fitted a CdTe empirical pseudopotential with a band gap of 1.54 eV, effective mass of $0.125m_e$ (where m_e is the free electron mass), and spin-orbit splitting of 0.87 eV. The conduction band and valence band deformation potentials of the pseudopotential are fitted to *ab initio* results.[13] The band edge states of the tetrapod under various compressive loads are calculated using the folded spectrum method[14] based on this empirical pseudopotential Hamiltonian.

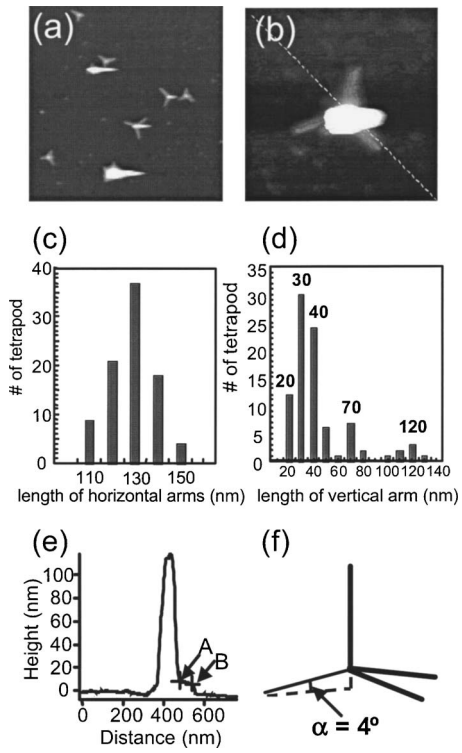

FIG. 1. (a) Tapping mode AFM image (2.4×2.4 μm^2) showing several tetrapods on a silicon wafer. The bright spot near the tetrapod center is due to feedback response to mechanical instabilities. (b) Tapping mode image (600×600 nm^2) of a single tetrapod and cursor profile along the broken line (e). [(c) and (d)] Histogram of arm lengths found in the images. The histogram shows that tetrapods with long vertical arms (~120 nm) are minority, the majority having heights in the range from 20 to 50 nm and a few with a length of 70 nm. (f) Model geometry derived from the height profile. The slope of the near horizontal arms (from A to B) is small, about 4°, indicating that the center of the tetrapod is separated from the substrate by 7–9 nm.

III. RESULTS

A. Geometrical structure of the tetrapods on Si wafers

Figure 1(a) shows 2.4×2.4 μm^2 tapping mode images of isolated tetrapods on a silicon wafer. The tetrapods are standing upright with three arms contacting the surface and the fourth arm pointing vertically out. Instabilities in the feedback control were observed during tapping to the tip of the arm, which give rise to the bright spot in the images near the center of the tetrapod. This instability might be related with the easy bending deformation of the long arm. The length of the three base arms was found to be 130 ± 10 nm [see histogram in Fig. 1(c)], while the vertical arm was about 120 nm. However, tetrapods with four long and nearly equal arms like those in Figs. 1(a) and 1(b) were found to be uncommon. More often the images revealed tetrapods with a substantially shortened vertical arm. The most commonly observed height was 30 ± 5 nm, followed by $40(\pm5)$ nm,

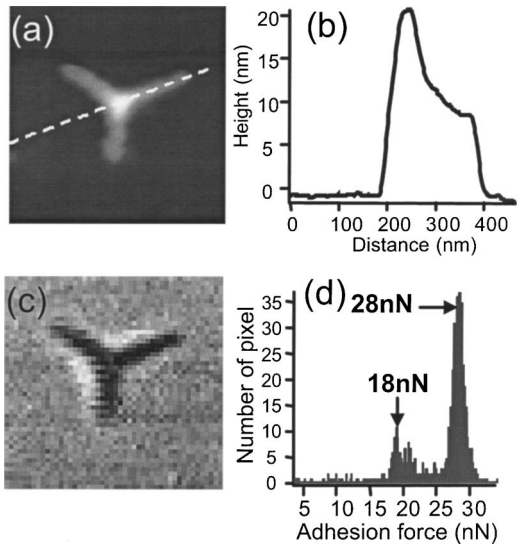

FIG. 2. (a) Topographic image of a tetrapod with a height of 25 nm, and height profile (b). (c) Adhesion force map extracted from the pull-off forces in a 64×64 pixel force-volume experiment. (d) Histogram of adhesion forces showing a bimodal distribution.

20(±5) nm, and 70(±5) nm, as shown in the histogram in Fig. 1(d). Since the core of the tetrapod is 10–15 nm above the surface, the actual arm length is also shorter by that amount. An image of the more common short arm tetrapod is shown in Fig. 2(a). We hypothesize that fracture of the vertical arm occurs as a result of capillary forces acting while drying.

Line profiles over tetrapods both long and short [Figs. 1(e) and 2(b)] show that the base arms are closer to the substrate than expected from a perfect tetragonal geometry. The slope of the arm between point A and B is about 0.06, corresponding to an angle with the substrate of ~4° [Fig. 1(f)]. This value should be compared with 19.5° expected for undistorted tetrahedrons. In this geometry the gap between the center of the tetrapod and the substrate is about 10 nm. The distortion is probably the result of strong attractive forces with the substrate that bend the arms and increase the contact length.

B. Mechanical properties

The mechanical response of the tetrapods to applied loads was investigated using FV mapping with a pixel density chosen so that at least one force-distance curve is taken over the top of the vertical arm in each tetrapod. An adhesion or pull-off force map from these curves is shown in Fig. 2(c). The adhesion of the tip is lower on the tetrapods (by about 10 nN, see histogram in Fig. 2(d)), than on the silicon substrate. This is not surprising because (a) the tetrapods are covered by a layer of trioctylphosphine oxide and octadecylphosphonic acid, which terminate with hydrophobic and weakly interacting CH_3 groups while the Si substrate is hydrophillic, so that in air an additional capillary adhesion force is present; (b) the contact area between the AFM tip and the tetrapods is small because the tip radius is about 40–60 nm and the arms have a diameter of 8 nm.

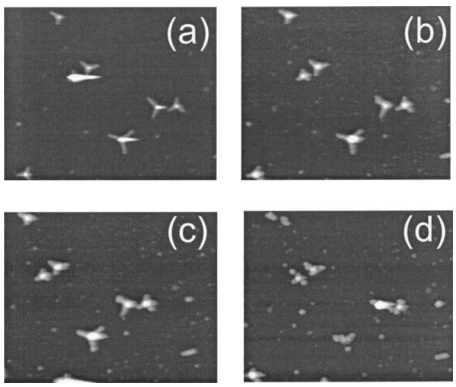

FIG. 3. Tapping mode AFM images (2.4×2.1 μm^2). (a) Initial image before application of forces. The tetrapod heights vary between 30 and 60 nm. (b) After a FV scan with maximum load of 50 nN. (c) After a FV scan at 90 nN. (d) Same after 130 nN. At this load the base arm structure is damaged.

To determine the elastic or inelastic response of the tetrapods, we performed experiments at increasing values of the maximum load. Figure 3(a) shows a 2.4×2.1 μm^2 tapping mode image of an area containing several tetrapods, with vertical arm lengths in the range of 30–60 nm. After an FV experiment with maximum load of 50 nN, the same area was reimaged and is shown in Fig. 3(b). The tetrapods appear broader now due to an increase in the tip radius. It was often found that sharp tips (<10 nm radius) giving the highest resolution images break easily upon application of forces above a few tens of nanonewtons. The heights are now close to 25 nm, indicating that loads of 50 nN are sufficient to break the vertical arm. Since the contact area between tip and tetrapod is essentially determined by the diameter of the vertical arm (8 nm), the ratio $50\ \text{nN}/\pi(4\ \text{nm})^2 = \sim 1$ GPa puts a higher bound to the elastic deformation limit of shortened vertical arms. A second FV experiment was performed with maximum load of 90 nN. Figure 3(c) shows an image obtained after this experiment. Except for some drift, the image is similar to the previous one and the height of the tetrapod is unchanged. However, as the applied force continues to increase the rest of tetrapod structure finally collapses. This occurred after the third FV experiment at a load of 130 nN. Figure 3(d) shows the image obtained after such experiment.

More quantitative observations can be made by examination of individual force-distance curves, as shown in Fig. 4. In these curves the origin of distances was arbitrarily placed at the minimum of the approach curve. The initial height of the tetrapod in the image of Fig. 4(a) (enclosed in a circle) was 25 nm. Three force-separation curves on top of the tetrapod with maximum load values as in the previous experiment (50, 90, and 130 nN) were obtained and are shown in Figs. 4(b)–4(d). Separation (x axis) in these curves is defined as the difference between the advance of the sample and the bending of the lever, thus corresponding to actual compression of the sample. At a load of 50 nN [Fig. 4(b)], the tetrapod has been compressed by 4 nm. The retract curve in the same graph shows some hysteresis as well as a higher adhesion (pull off) force. After release of the load the height recovered to 25 nm. The difference between the height under compression and the height under zero load

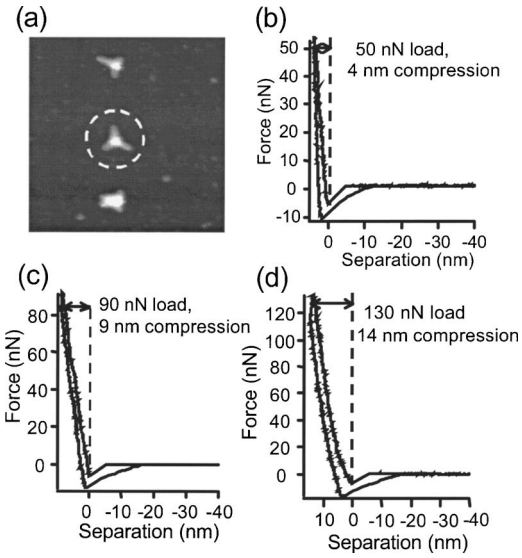

FIG. 4. (a) Tapping mode image (1.5×1.5 μm^2) containing three tetrapods with heights of 24, 25, and 25 nm. [(b)–(d)] Force-separation curves taken over the center of the tetrapod marked by the white circle in (a). The maximum loads are 50, 90, and 130 nN in each curve, respectively, which produced compressions of 4, 9, and 14 nm respectively.

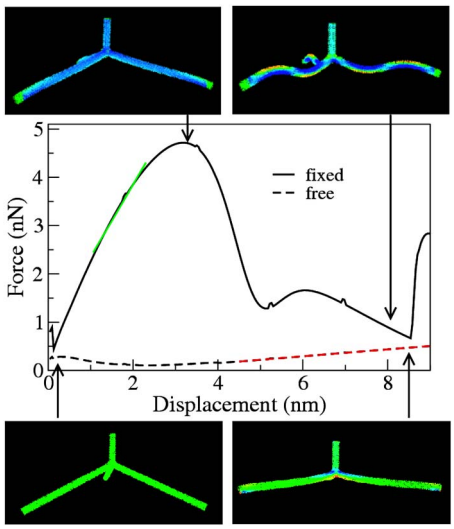

FIG. 5. (Color online) Calculated force-displacement relationship. The figures represent the tetrapods with color code to indicate local hydrostatic strain at each atom site. Green means zero hydrostatic strain, red means tensile strain, and blue means compressive strain. The dashed line in the graph at the center corresponds to the free sliding arm case (bottom figures); the solid line corresponds to the fixed end arm case (top figures). The tetrapod used in the calculations is three times smaller in each dimension than the ones used in the experiment. The green line in the force curve indicates where the linear fitting of the spring constant is performed.

(4 nm) corresponds to the elastic deformation, which can be attributed to flattening of the pyramid formed by the three base arms. The spring constant for this tetrapod deformation mode can thus be estimated to be 50 nN/4 nm=12.5 N/m.

When the maximum load was 90 nN in the second FV experiment, the force-separation curve on the same tetrapod shows a compression of 9 nm. After release of the load the height recovered again to its initial value of 25 nm. We attribute the 9 nm elastic deformation again to flattening of the base of the pyramid. The same simple arithmetic calculations as before gives a spring constant of 90 nN/9 nm=10 N/m, not too far from the previous estimate.

The third FV experiment to a maximum load of 130 nN produced a compression of 15 nm. As shown in Fig. 3 these high load values produced irreversible damage to the base arms of the tetrapod. A higher limit for the plastic yield stress for this deformation can thus be set to 130 nN/π(4 nm)^2 =2.6 GPa.

Our first simulation considered the case of a tetrapod in which the horizontal base arms are allowed to freely move along the surface, shown as the dashed line in Fig. 5. The force increases linearly as the base arms are completely flattened against the surface, with a calculated spring constant of 0.07 N/m. In the inset figures, we depict representative structures from these simulations, color coding the local hydrostatic strain at each atom site. The greatest compressive and expansive changes occur near the core joining the arms together, and the horizontal base arms are relatively uncompressed except near the tip. Scaling the spring constant by 3 (as discussed in Sec. II B) gives a result of 0.25 N/m, which is ~50 times smaller than the experimental value. Since the AFM imaging performed in Sec. III A might not resolve an enlarged zinc-blende core of the tetrapod, we have examined how this might change the forces. Increasing the diameter of the zinc-blende core by as much as a factor of 1.5 (while keeping the diameter of the arms fixed) did not alter the force behavior significantly, so we eliminate this possibility.

Next we examined the case in which the horizontal base arm ends were fixed horizontally in place, as might result from the strong sticking interaction with the substrate mentioned in Sec. III A. The results of this simulation are shown as the solid line in Fig. 5. Unable to slide along the surface, the horizontal arms undergo an S-shaped buckling, as shown in the top right inset of Fig. 5. For displacements up to ~3.3 nm, this would correspond to a spring constant of 1.5 N/m, leading to a scaled spring constant for the tetrapod of ~4.5 N/m, which is more consistent with the experimental results than the freely sliding case. Beyond 3.3 nm displacement, the force is observed to be reduced, but this probably corresponds to the plastic regime observed in the experiment and would be accompanied by other structural effects which are beyond the scope of our elastic simulations. The fact that our calculated spring constant is about a factor of 2 smaller than the experimental one might have several causes. One possible reason is that in our calculation, we have ignored any capillary force between the tetrapod and the substrate. Such capillary force could flatten the lower part of the tetrapod legs, thus effectively reducing their length while increasing the spring constant.

C. Electrical conductance of tetrapods under load

Figure 6(a) shows a topographic image of a region in a Au film containing a tetrapod. Its vertical arm is 23 nm high. Using a conductive TiN-coated tip, the current through the tetrapod was measured as a function of applied bias,[15] with the tip contacting the top of the tetrapod's vertical arm at a load below 0 nN (i.e., pulling the tip away from the surface but still in the attractive well). The current bias characteristic

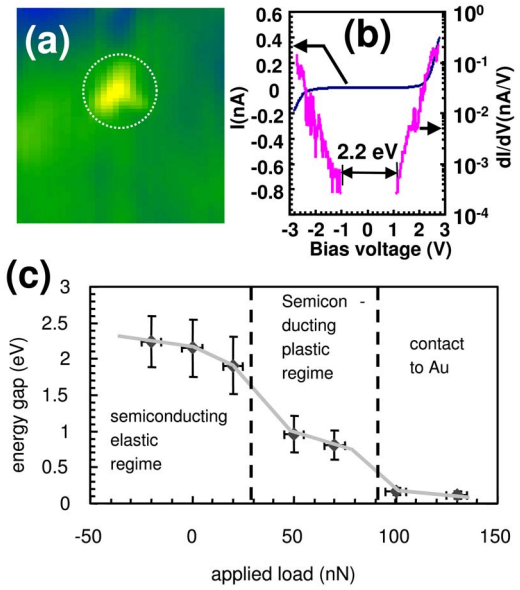

FIG. 6. (Color online) (a) Contact mode AFM topographical image ($1.0 \times 1.0\ \mu m^2$) obtained in ultrahigh vacuum, of a Au(111) oriented film with a tetrapod deposited near the center (marked by a circle). The height is 25 nm. (b) Current-voltage (I-V) and dI/dV plots at an effective applied load of 0 nN showing an apparent gap in the current of 2.2 eV. (c) Plot of current gap width as a function of effective applied load. In the left region the tetrapod deforms elastically by flattening of the pyramidal base. In the center region the load causes the tetrapod arms to be flattened against the substrate. The right hand region corresponds to damage of the tetrapod and tip-gold metallic contact.

under this condition is shown in Fig. 5(b), both in I-V and dI/dV forms (the latter in a log scale). These I-V curves were quite reproducible, indicating that the contact is elastic at these loads. The current became immeasurably small (<0.1 pA) when the applied voltage between tip and gold decreased below ±1.1 V. This 2.2 eV range of current gap is higher than the optical band gap of CdTe (1.6–1.8 eV) reported by Manna *et al.*[16] In general, the measured current gap is not necessarily equivalent to the semiconductor energy gap because in a diode configuration the field distribution in the gap between tip and gold electrodes is unknown. In addition, Schottky barriers and poorly defined interfaces of the electrodes with the surfactant covered tetrapods make the 2.2 eV current gap an upper limit of semiconductor energy gap.

This gap was found nonetheless to depend on applied load, as shown in Fig. 6(c). For small elastic deformations, i.e., for effective loads below 50 nN (pressure <1 GPa), the gap remains approximately constant. Between 50 and 70 nN, when the pyramidal structure is elastically flattened, the gap decreases to about 0.9 eV. Finally, at high load (>100 nN), the I-V measurement shows a metallic character, suggesting that the tetrapod has been damaged and that the tip contacts the gold substrate. This is consistent with the observation in Fig. 3(d) where the horizontal arms were damaged by a load of 130 nN.

We have calculated the conduction band minimum (CBM) and valence band maximum (VBM) states using the empirical pseudopotential Hamiltonian. We have calculated three loading situations: one with zero load (bottom left inset in Fig. 5, to be called free tetrapod below); one at the maximum load with fixed arm ends (top left inset in Fig. 5, to be called fixed arm tetrapod below); and one with the arms touching the substrate in the free sliding case (bottom right inset in Fig. 5, to be called free sliding flattened tetrapod below). The VBM energies for these three cases are −3.997, −3.965, and −4.017 eV, respectively, while the CBM energies for these three cases are −2.002, −1.911, and −1.957 eV, respectively. Thus the band gap changes from 1.995 eV in the free tetrapod to 2.054 eV in the fixed arm tetrapod to 2.06 eV in the free sliding flattened tetrapod. The VBM and CBM wave functions for the free tetrapod and the free sliding flattened tetrapod are plotted in Fig. 7, while the wave function plots for the fixed arm tetrapod are very similar to that of the free tetrapod. For this reason they are not shown here. We see that both VBM and CBM wave functions are localized near the core of the tetrapod, except for the CBM of the free sliding flattened tetrapod, where 70% of the weight of the charge density is located at the arms. The CBM+1 state in the free tetrapod is found to be located at the three arms[17] and it has the same symmetry as the CBM at the core. In the free sliding tetrapod, the core region has a strong compressive hydrostatic strain, which raises the energy of the original CBM at the core. As a result, this CBM and the CBM+1 states hybridize and form the current CBM with both core and the arm charge. It is at an anticrossing transition stage of these two states. Thus our calculation indicates that it might be possible to use mechanical load to cause state crossing. Note that for larger tetrapods (as in the experiments reported here), this state crossing becomes easier since the original CBM to CBM+1 energy difference is smaller, but the strain effects remain the same. It will be interesting to measure such state crossing experimentally in the future since it corresponds to a significant photoluminescence optical signal change.

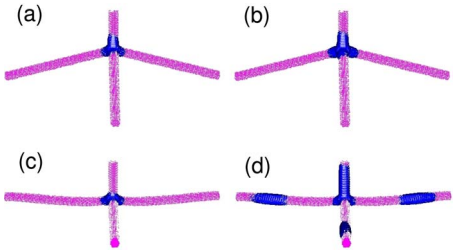

FIG. 7. (Color online) Wave function isodensity plots (shown in blue) of conduction band minimum (CBM) states [(b) and (d)] and valence band maximum (VBM) states [(a) and (c)], for uncompressed tetrapods [(a) and (b)] and compressed free sliding flattened tetrapods [(c) and (d)]. The same isosurface value is used in all plots.

The calculated band gap change, from 1.995 to 2.06 eV, is due to the internal strain of the tetrapod caused by the application of load. It does not explain the large experimental current band gap changes observed in Fig. 6(c), and it has the wrong sign (band gap increases, instead of decreasing). One possible reason for the current band gap decreasing is due to the polarization potential $P(r)$ in the quasiparticle equation.[18] $P(r)$ is defined as $0.5\Sigma_{r'\to r}[W(r',r)-W_b(r',r)]$, where $W(r',r)$ is the screened potential at r' of a point charge at r in the given system, and $W_b(r',r)$ is the same screened po-

tential in an infinite bulk. It has been shown that[18] $P(r)$ needs to be added (subtracted) to the pseudopotential Hamiltonian to get the quasiparticle equation for the electron (hole). In the above calculation, $P(r)$ is not included. However, due to the existence of the metallic substrate, there could be a large negative $P(r)$. Since the wave functions are localized near the core, the magnitude of $P(r)$ at the core can provide an estimate for the eigenenergy change. For a metallic substrate $P(r)$ is caused by the image charge. Thus, if the height of the core is h, $P(r)=-1/4h$ and the change in the quasiparticle band gap is $2P(r)=-1/2h$. A typical tetrapod will have $h=25$ nm when ~20 nN negative load is applied, this will yield a band gap reduction of ~30 meV. When large load (~30 nN) is applied [near the limit of the elastic regime in Fig. 6(c)], the core of the tetrapod is probably close to make contact with the substrate. Then $h=4$ nm for an 8 nm diameter tetrapod. This will give a band gap reduction of ~0.2 eV. This can be used to explain the ~0.2 eV band gap reduction in the elastic regime of Fig. 6(c). After the tetrapod completely contacts the substrate [perhaps, in the plastic regime of Fig. 5(c)], the above perturbation argument might no longer hold, and more detailed calculations based on the $P(r)$ added to Schrodinger's equation become necessary. In those cases, the wave function might become further localized due to $P(r)$ and make the band gap even smaller, which might correspond to the big band gap drop in the plastic regime shown in Fig. 6. Other plastic changes of the tetrapod shape and atomic structure can also cause large changes in the band gap.

IV. CONCLUSIONS

We have used AFM to study the mechanical and electronic properties of individual tetrapod-shaped CdTe nanocrystals. The tetrapods were found to be very fragile, and many "as deposited" tetrapods have their vertical arm considerably shortened, fractured we believe by capillary forces during solvent evaporation. We also found that such fracture events result in a distribution of vertical heights with the most commonly found values being 30, 40, 20, 70, and 120(±5) nm.

We have shown that the vertical arm can be also broken by the AFM tip when the applied force reaches a few tens of nanonewtons. An upper limit of 1 GPa was found for the elastic-inelastic threshold leading to tetrapod fracture. After the vertical arm is reduced to a few tens of nanometers, the remaining pyramidal structure behaves as a spring with a constant of approximately 10 N/m. The deformation occurs by flattening of the pyramid while maintaining the base arms intact. The tetrapod structure (horizontal arms) collapses at pressures above 2.6 GPa. Our simulations indicate that the substrate plays an important role in determining the spring properties in the elastic regime, depending on whether or not the ends of the arms are allowed to slide freely. By comparing the calculated and the observed spring constants, we concluded that the ends of the arms are probably stuck during the compression process.

Electrical transport measurements of tetrapods on a gold substrate indicate that they behave as semiconductors with an apparent energy gap of 2.2 eV or less at pressures below 1 GPa (corresponding to a 50 nN load). This gap decreases to about 0.9 eV in the pressure range of 1–2 GPa (60–110 nN loads), when the pyramidal structure is deformed. At higher loads, the contact has a metallic character due to the tip making contact with the gold substrate. Atomistic quantum mechanical calculations show that band gap changes due to the elastic deformation of the tetrapod are much too small to explain the observed change in the elastic regime. Instead, an electrostatic polarization potential due to the image charge on the metallic substrate might explain the observed large band gap reduction. Our calculations also indicate that mechanical loads might be used to induce electron state crossing in the tetrapod.

ACKNOWLEDGMENTS

This work was supported by the Director, Office of Energy Research, Office of Basic Energy Sciences, Molecular Foundry, Materials Sciences Division, of the U.S. Department of Energy through the Lawrence Berkeley National Laboratory, Contract No. DE-AC02-05CH11231. The calculations were performed using the resources of the National Energy Research Scientific Computing Center. The authors thank Dr. Peter Graf and Dr. Qingzhong Zhao (National Renewable Energy Laboratory) for providing the code to generate the uncompressed tetrapod geometries.

[1] J. S. Liu, T. Tanaka, K. Sivula, A. P. Alivisatos, and J. M. J. Frechet, J. Am. Chem. Soc. **126**, 6550 (2004).
[2] D. J. Milliron, S. M. Hughes, Y. Cui, L. Manna, J. B. Li, L. W. Wang, and A. P. Alivisatos, Nature (London) **430**, 190 (2004).
[3] L. W. Wang, J. Phys. Chem. B **109**, 23330 (2005).
[4] J. B. Li and L. W. Wang, Appl. Phys. Lett. **85**, 2929 (2004).
[5] H. Yu, J. B. Li, R. A. Loomis, L. W. Wang, and W. E. Buhro, Nat. Mater. **2**, 517 (2003).
[6] E. A. Hassan, W. F. Heinz, M. D. Antonik, N. P. D'Costa, S. Nageswaran, C. A. Schoenenberger, and J. H. Hoh, Biophys. J. **74**, 1564 (1998).
[7] M. Radmacher, M. Fritz, J. P. Cleveland, D. A. Walters, and P. K. Hansma, Langmuir **10**, 3809 (1994).
[8] C. Rotsch and M. Radmacher, Langmuir **13**, 2825 (1997).
[9] J. Y. Park, R. J. Phaneuf, D. F. Ogletree, and M. Salmeron, Appl. Phys. Lett. **86**, 172105 (2005); J. Y. Park, D. F. Ogletree, M. Salmeron, C. J. Jenks, and P. A. Thiel, Tribol. Lett. **17**, 629 (2004).
[10] J. E. Sader, J. W. M. Chon, and P. Mulvaney, Rev. Sci. Instrum. **70**, 3967 (1999).
[11] A. J. Williamson, L. W. Wang, and A. Zunger, Phys. Rev. B **62**, 12963 (2000).
[12] *Semiconductors, II-VI and I-VII Compounds: Semimagnetic Compounds*, edited by U. Rossler, Landolt-Bornstein, New Series, Group III, Vol. 41B (Springer, Heidelberg, 1999).
[13] S.-H. Wei and A. Zunger, Phys. Rev. B **60**, 5404 (1999).
[14] L. W. Wang and A. Zunger, J. Chem. Phys. **100**, 2394 (1992).
[15] J. Y. Park, D. F. Ogletree, P. A. Thiel, and M. Salmeron, Science **313**, 186 (2006).
[16] L. Manna, D. J. Milliron, A. Meisel, E. C. Scher, and A. P. Alivisatos, Nat. Mater. **2**, 382 (2003).
[17] J. Li and L. W. Wang, Nano Lett. **3**, 1357 (2003).
[18] L. W. Wang, J. Phys. Chem. B **109**, 23330 (2005).